

An S-scheme heterojunction of single Ni sites decorated ultrathin carbon nitride and Bi₂WO₆ for highly efficient photothermal CO₂ conversion to syngas

Jiaming Wu ^a, Keyan Li ^{a,*}, Sufeng An ^{a,b}, Siyang Yan ^a, Jiaxu Liu ^a, Chunshan Song ^{a,c}, Xinwen Guo ^{a,*}

^a State Key Laboratory of Fine Chemicals, Frontiers Science Center for Smart Materials, PSU-DUT Joint Center for Energy Research, School of Chemical Engineering, Dalian University of Technology, Dalian 116024, China

^b SINOPEC Dalian Research Institute of Petroleum and Petrochemicals Co., Ltd., Dalian 116045, China

^c Department of Chemistry, Faculty of Science, The Chinese University of Hong Kong, Shatin 999077, Hong Kong, China



ARTICLE INFO

Keywords:
CO₂ reduction
Photothermal catalysis
Heterojunction
Ultrathin carbon nitride
Syngas

ABSTRACT

Solar-driven conversion of CO₂ and H₂O to value-added chemicals or fuels is an ideal strategy to tackle the energy crisis and environmental issues. However, construction of highly efficient photosynthesis systems remains a challenge. This work reports a heterojunction catalyst consisting of ultrathin carbon nitride with single Ni sites and Bi₂WO₆ for photothermal conversion of CO₂ and H₂O to syngas. The catalyst exhibits exceptional activity at medium temperature of 250 °C, with CO and H₂ production rates of 4493 and 9191 μmol g⁻¹ h⁻¹, respectively. Experimental results and DFT calculations reveal that the construction of S-scheme heterojunction and the introduction of single Ni sites greatly improve the separation of photogenerated carriers as well as the adsorption and activation of CO₂. Meanwhile, it is proved that light drives the generation of H⁺ and activates the CO₂ molecules, while heat accelerates the generation and diffusion of H⁺. The photothermal synergistic effect promotes the catalyst activity by two orders of magnitude.

1. Introduction

Nowadays, in order to cope with the increasing energy crisis and environmental problems, the conversion of CO₂ into value-added chemical feedstocks or fuels is one of the goals of modern catalysis [1, 2]. Syngas, a mixture of CO and H₂, is a useful feedstock for producing liquid fuels and synthetic products. Ideally, the CO₂ reduction and water splitting reactions can be combined for generation of syngas by artificial photosynthesis [3,4]. However, due to the chemical inertness of CO₂ molecules and the high photogenerated carrier recombination rate of single semiconductors, most photocatalytic CO₂ reduction reactions still rely on the help of sacrificial agents such as methanol and triethanolamine, or expensive photosensitizers such as bipyridine ruthenium to achieve a desirable performance. Although there have been many efforts attempting to carry out the CO₂ photoreduction reaction without using sacrificial agents or photosensitizers, the low conversion efficiency still prevents it from practical applications.

In recent years, the strategy of utilizing the photothermal coupling

effect to catalyze reactions such as CO₂ reduction or water splitting has become particularly attractive. In the process of photothermal catalysis, on one hand, photocatalysis can effectively reduce the activation energy of the reaction by exciting photogenerated carriers and thus inducing the generation of new reaction intermediates. On the other hand, by providing additional thermal energy, the charge kinetics and the mass transport of the reaction can be greatly accelerated, leading to the increased reaction rate [5,6]. As a result, photothermal catalysis can override the chemical inertness of inactive molecules such as CO₂ at moderate temperatures and achieve product yields far exceeding those of photocatalysis [7,8]. Therefore, when a photocatalyst has the required thermal stability for photothermal catalysis, replacing the sacrificial agent or photosensitizer by heating is a low-cost and convenient strategy to greatly improve the efficiency of a photocatalytic process [9].

Polymeric carbon nitride (PCN) with a π-conjugated system is now widely utilized in photocatalysis due to its suitable energy band structure, great potential for modification, and convenience of preparation

* Corresponding authors.

E-mail addresses: keyanli@dlut.edu.cn (K. Li), guoxw@dlut.edu.cn (X. Guo).

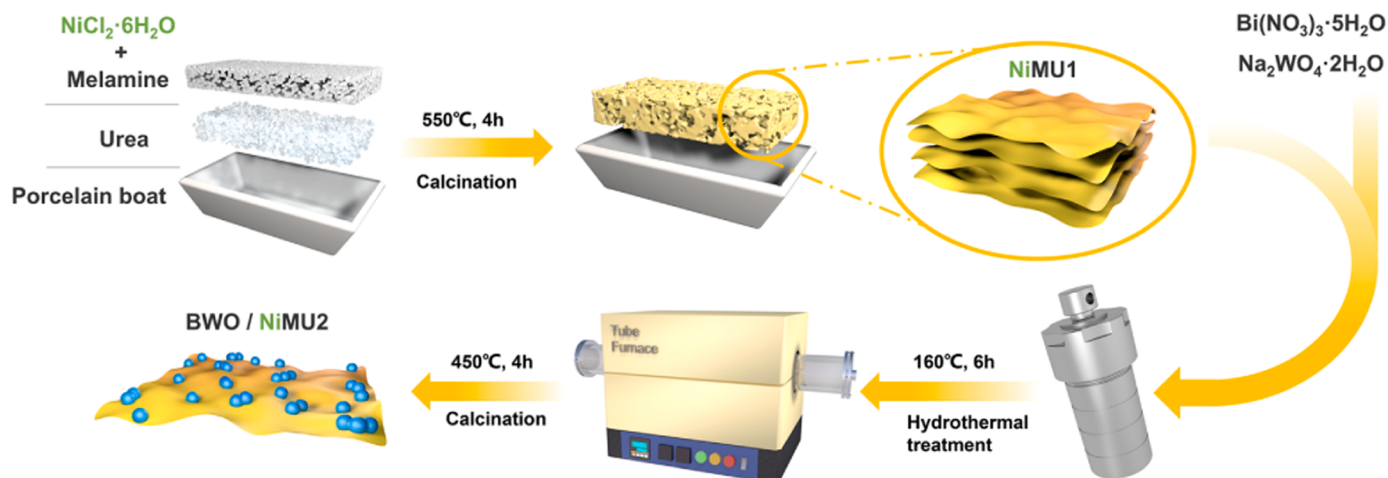


Fig. 1. Schematic illustration of the synthesis of BWO/NiMU2 heterojunctions.

[10,11]. Meanwhile, since PCN contains a large number of N atoms with pore-oriented lone electron pairs, it provides abundant and homogenous coordination sites for anchoring and dispersing metals [12]. The metal atoms such as Ni, Co and Cu that are anchored in PCN can not only modulate its electronic structure and thus improve the charge separation efficiency, but also act as active sites for adsorption and activation of reactants in the photocatalytic reactions [13,14]. Therefore, the introduction of highly dispersed metals into PCN is a facile and effective strategy to improve its photocatalytic activity.

Generally, PCN prepared with urea as precursor has a larger specific surface area but more surface carbon defects than those prepared with melamine [15,16]. Although the latter has higher crystallinity as well as better thermal stability, the ultra-low specific surface area is still a major limitation to its performance. Preparation of PCN simultaneously possessing large surface area, high crystallinity and good thermal stability is quite promising but remains a challenging task. Moreover, considering the oxidation of water is a rate-limiting step in artificial photosynthesis since it is a kinetically hindered reaction [17], combining PCN with an oxidation-type semiconductor to construct a heterojunction is a feasible strategy to achieve high-efficiency overall reaction between CO_2 and H_2O . Among all the oxidation-type semiconductors, Bi_2WO_6 , an Auri-villius phase double perovskite oxide, is an ideal candidate for construction of such a heterojunction with PCN due to its narrow band gap, relatively positive valence band potential as well as superior chemical and thermal stability [18–20].

In this work, we prepared melamine-based ultrathin crystalline PCN nanosheets by a unique two-layer calcination method, and constructed $\text{Bi}_2\text{WO}_6/\text{PCN}$ step (S)-scheme heterojunction via in-situ hydrothermal method and secondary calcination. This heterojunction material exhibits high activity in the photothermal CO_2 reduction reaction. The introduction of atomically dispersed Ni sites in PCN further improves the catalyst activity and adjusts the ratio of produced CO and H_2 . The S-scheme charge transfer route was demonstrated, and the mechanisms underpinning the high activity of the catalyst in photothermal CO_2 conversion were revealed.

2. Experimental section

2.1. Materials

All chemical reagents were purchased and used directly without further purification. Urea (99%, AR) and $\text{Bi}(\text{NO}_3)_3 \cdot 5\text{H}_2\text{O}$ (99%, AR) were purchased from Tianjin Damao Chemical Reagent Factory. Melamine (99%, AR), mannitol (99%, AR) and $\text{Na}_2\text{WO}_4 \cdot 2\text{H}_2\text{O}$ (99%, AR) were purchased from Tianjin Guangfu Fine Chemical Research Institute. $\text{NiCl}_2 \cdot 6\text{H}_2\text{O}$ (99%, AR) was purchased from Shenyang Xinxing Chemical

Reagent Factory. CO_2 (99.999%) and Ar (99.999%) were purchased from Dalian Institute of Chemical Physics.

2.2. Synthesis of PCNs

In a typical synthesis process, melamine-based ultrathin PCNs were prepared by a unique two-layer calcination method. First, 2 g of urea was spread flat on the bottom of a porcelain boat, followed by an equal mass of melamine spread flat on the urea. The porcelain boat was wrapped tightly with tinfoil and then calcined in a muffle furnace at 550°C for 4 h. After cooling to room temperature, the obtained yellowish fluffy powder was noted as MU1. After grinding, MU1 was placed in a porcelain boat and some holes were punched out after being wrapped with tinfoil. Subsequently, it was calcined in a tube furnace under air atmosphere at 450°C for 4 h and the sample obtained was denoted as MU2.

For the preparation of PCN with single Ni sites, the melamine was replaced by a mixture of 2 g of melamine and x mg of $\text{NiCl}_2 \cdot 6\text{H}_2\text{O}$, and the samples were denoted as xNiMU1 and xNiMU2 ($x = 1, 3, 5$) through primary and second calcinations, respectively.

For comparison, the samples obtained after primary and secondary calcinations using only melamine as a precursor were denoted as M1 and M2. Accordingly, the samples obtained using only urea as a precursor were denoted as U1 and U2.

2.3. Synthesis of BWO/NiMU2

In a typical synthesis, 0.24 g of $\text{Bi}(\text{NO}_3)_3 \cdot 5\text{H}_2\text{O}$ and 0.08 g of $\text{Na}_2\text{WO}_4 \cdot 2\text{H}_2\text{O}$ were dissolved in 15 mL of mannitol solution (0.1 M), followed by the addition of 1 g of MU1. The suspension was stirred homogeneously and then hydrothermally reacted at 160°C for 6 h. The resulting precipitate was calcined in a tube furnace under air atmosphere for 4 h after being heated to 450°C . Finally, the obtained yellow powder was denoted as 1BWO/MU2. The synthesis of pure Bi_2WO_6 (abbreviated as BWO) was similar to the above process without the addition of MU1.

The samples yBWO/MU2 ($y = 0.1, 0.25, 0.5, 0.75$) with different amount of BWO were obtained by proportionally scaling down the amount of metal salts. The nickel contents were optimized by replacing MU1 with xNiMU1 during the preparation of 0.5BWO/MU2, and the samples obtained were denoted as 0.5BWO/xNiMU2 ($x = 1, 3, 5$).

Details of material characterizations, photothermal CO_2 reduction performance tests and DFT calculation methods can be found in the Supporting Information.

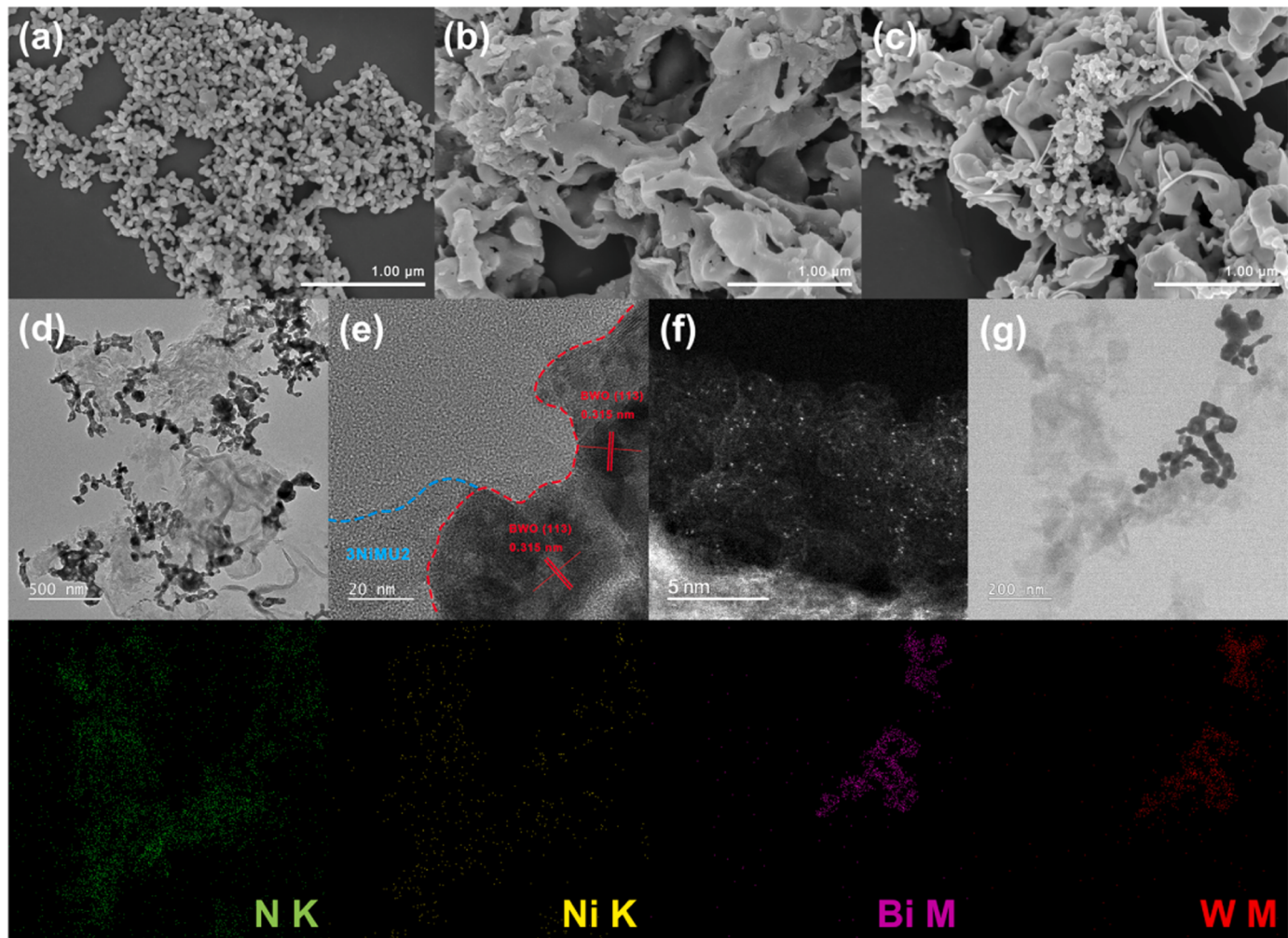


Fig. 2. SEM images of (a) BWO, (b) 3NiMU2 and (c) 0.5BWO/3NiMU2; (d) TEM image, (e) HRTEM image and (f) HAADF-STEM image of 0.5BWO/3NiMU2; (g) Elemental mapping images of N (green), Ni (yellow), Bi (purple) and W (red).

3. Results and discussion

3.1. Composition, structure and morphology of BWO/NiMU2 heterojunctions

We first explored the preparation of a PCN material with high photocatalytic activity and good thermal stability. From Fig. S2 and S3, by using melamine as a precursor and urea as a self-sacrificial gas template, MU1 nanosheets were obtained through a unique two-layer calcination method. Further, ultrathin MU2 nanosheets were obtained by thermal stripping treatment (Fig. S4). Compared to the M2 and U2 prepared by using melamine and urea as precursors, respectively, MU2 has thinner thickness of 2.15 nm (Figs. S5), larger specific surface area of $137.8 \text{ m}^2 \text{ g}^{-1}$ (Fig. S6) and higher crystallinity (Fig. S7). Therefore, MU2 exhibits much higher photocatalytic activity of CO_2 reduction with H_2O (Fig. S8). Moreover, MU2 has comparable thermal stability with the melamine-derived sample M2 (Fig. S9), which allows it to be utilized in further photothermal catalysis.

The synthesis of BWO/NiMU2 heterojunctions first required the introduction of single Ni sites during the synthesis of MU1, and the resulting sample was named as NiMU1. BWO was then hydrothermally grown on the surface of NiMU1. Finally, the two components were calcined in an air atmosphere to obtain the heterojunction material (Fig. 1). This in-situ growth of BWO on PCN and the second calcination ensure an intimate interfacial contact for the heterojunction. The 0.5BWO/3NiMU2 sample that shows the best performance in the

subsequent photothermal CO_2 conversion was selected as an example for characterizations.

From the X-ray diffraction (XRD) patterns in Fig. S10a, 3NiMU2 also shows two characteristic diffraction peaks of PCN at 13.0° and 27.8° , which indicates that the introduction of Ni sites does not destroy the structure of PCN. For the heterojunction materials 0.5BWO/MU2 and 0.5BWO/3NiMU2, besides the presence of the characteristic diffraction peak of PCN at 27.8° , the peak at 28.3° , corresponding to the (113) crystal plane of BWO (JCPDS No. 39-0256) [21,22], can be also observed. The FT-IR spectra of the samples are shown in Fig. S10b. For pure BWO, the peaks at 538 cm^{-1} and 739 cm^{-1} correspond to the stretching vibrations of the Bi–O and W–O bonds, respectively [23]. For MU2 and 3NiMU2, the sharp peak at 810 cm^{-1} is caused by the breathing vibration of the triazine unit in PCN, while a series of peaks within $1230 - 1630 \text{ cm}^{-1}$ correspond to the C–N and C=N stretching modes in the heterocyclic compounds [24]. The presence of all the above peaks in the spectra of 0.5BWO/3NiMU2 indicates the successful combination of BWO and PCN in the heterojunction.

The morphology of 0.5BWO/3NiMU2 heterojunction was investigated by using scanning electron microscope (SEM), transmission electron microscope (TEM), and high-resolution TEM (HRTEM). As shown in Fig. 2a and b, pure BWO prepared by hydrothermal-calcination method is short rod-like nanoparticles, while 3NiMU2 has a thin nanosheet morphology. The former grows like a coral tuft on the surface of the latter (Fig. 2c and d). The lattice spacing of 0.315 nm belonging to the (113) crystal plane of BWO can be clearly observed in the HRTEM image

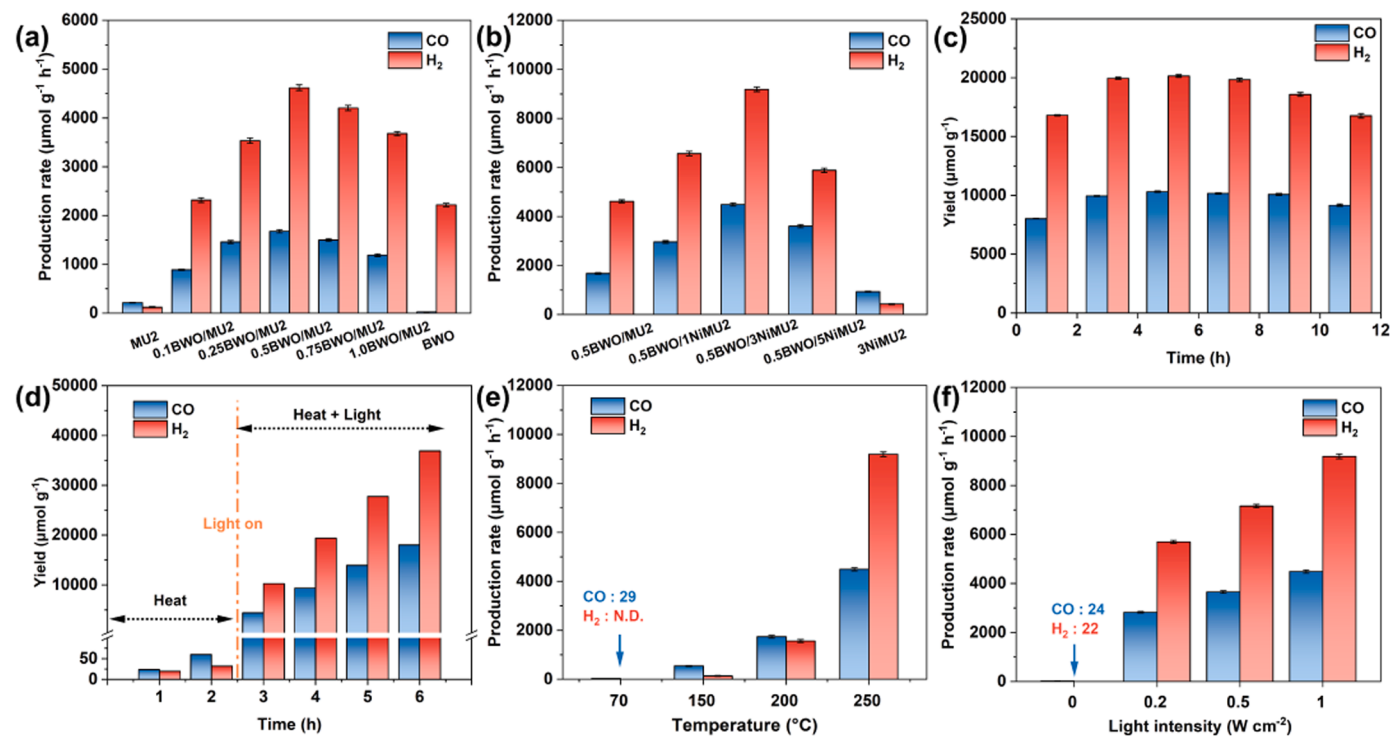


Fig. 3. Syngas production rates of (a) yBWO/MU2 heterojunctions (b) and 0.5BWO/xNiMU2 heterojunctions over a 4 h reaction; (c) Syngas yield of 0.5BWO/3NiMU2 per 2 h over 12 h (Reaction conditions: 250 °C, light intensity 1.0 W cm⁻²). (d) Time-dependent syngas yield of 0.5BWO/3NiMU2 for the thermally catalytic CO₂ conversion at 250 °C (0 – 2 h) and photothermally catalytic CO₂ conversion (2 – 6 h); Syngas production rates of 0.5BWO/3NiMU2 at (e) different temperatures and (f) different light intensities.

(Fig. 2e). The immobilization of Ni sites in the PCN is evidenced by the high-angle annular dark-field scanning transmission electron microscopy (HAADF-STEM) image. The clear and isolated bright spots in Fig. 2f indicate that the Ni sites are atomically dispersed. The high dispersion of Ni is attributed to the abundant N atoms in PCN that can anchor the transition metals. In addition, the uniform distribution of Ni sites in PCN can be also observed through the elemental mapping images (Fig. 2g). These results provide evidences for the atomic-level dispersion of Ni in PCN and the tight binding of BWO to PCN.

XPS spectra were used to study the chemical states of the surface elements as well as the charge transfer between components in the 0.5BWO/3NiMU2 heterojunction (Fig. S11). For the N 1 s XPS spectrum of MU2, the three peaks at 398.7, 400.1 and 401.2 eV originate from sp^2 hybridized nitrogen (C–N=C), tertiary nitrogen N–(C)₃ and free amino group (C–N–H), respectively [25,26], while the peak at 404.5 eV is derived from the π -excitation effect in the heptazine rings [27]. The N 1 s peaks of 3NiMU2 are shifted toward lower binding energy by 0.1 – 0.2 eV compared to MU2, indicating that the electrons transfer from the introduced Ni atoms to the N atoms. In the O 1 s XPS spectrum of BWO, the peak at 530.2 eV corresponds to the lattice oxygen, while the peak at 532.2 eV belongs to the surface-adsorbed oxygen species (e.g., H₂O) [28]. Compared to pure BWO, the O 1 s, Bi 4 f and W 4 f peaks of 0.5BWO/3NiMU2 are shifted to lower binding energies by 0.1 – 0.2 eV, while the N 1 s peaks of 0.5BWO/3NiMU2 are shifted to higher binding energies by 0.2 – 0.3 eV compared to 3NiMU2. This indicates that the electron density on 3NiMU2 decreases while that on BWO increases, demonstrating that electrons transfer from 3NiMU2 to BWO after the formation of an intimate heterojunction interface. In addition, the positions of the peaks in the O 1 s, Bi 4 f and W 4 f spectra of 0.5BWO/3NiMU2 are same to those of 0.5BWO/MU2, indicating that the introduction of Ni in MU2 just affects the electron density of MU2 but not that of BWO, and thus contributes little to the heterojunction interface.

3.2. Photothermal conversion of CO₂ and H₂O to syngas

Without any sacrificial agent or photosensitizers, the photothermal catalytic performance of pure BWO, MU2, 3NiMU2 as well as a series of yBWO/MU2 and 0.5BWO/xNiMU2 heterojunctions was evaluated. As shown in Fig. 3a, a small amount of CO (232 $\mu\text{mol g}^{-1} \text{h}^{-1}$) and H₂ (119 $\mu\text{mol g}^{-1} \text{h}^{-1}$) are detected when MU2 is used as the catalyst. Pure BWO, on the other hand, exhibits almost exclusively H₂ evolution activity. Interestingly, the syngas production rates of the yBWO/MU2 heterojunctions are much higher than that of MU2, and the CO and H₂ production rates of 0.5BWO/MU2 reach 1677 and 4618 $\mu\text{mol g}^{-1} \text{h}^{-1}$, respectively. In this case, the ratio of CO to H₂ in the syngas is in the range of 1:2.4 to 1:3.1.

Atomically dispersed Ni sites were introduced into the PCN to further improve the catalytic performance of the heterojunction. As shown in Fig. 3b, the contents of Ni are optimized and the 0.5BWO/3NiMU2 sample possesses the highest syngas yields with CO and H₂ production rates of 4493 and 9191 $\mu\text{mol g}^{-1} \text{h}^{-1}$, respectively, which are 4.8 and 21.3 times those of 3NiMU2. This syngas production rate significantly surpasses those of the CO₂ photoreduction systems with sacrificial agents and photosensitizers as well as photothermal CO₂ reduction systems (Table S1). Table S2 lists the product production rates of the BWO/NiMU2 catalysts. It is noteworthy that the introduction of Ni sites leads to increased proportion of CO in the syngas, resulting in the ratio of CO to H₂ between 1:1.6 and 1:2.2. Meanwhile, the BWO/NiMU2 catalysts have an over 95% selectivity for syngas.

The long-time photothermal catalytic performance (Fig. 3c) shows that the CO₂ conversion efficiency remains relatively stable for 12 h. More specifically, the yield per 2 h exhibits a small increase first and then a slight decrease. From the comparison of structure and morphology of the catalyst before and after reaction (Fig. S12) as well as the thermal stability test (Fig. S13), it is confirmed that the catalyst possesses good structural and thermal stability. The increase of activity in the second 2 h interval can be attributed to the induction period,

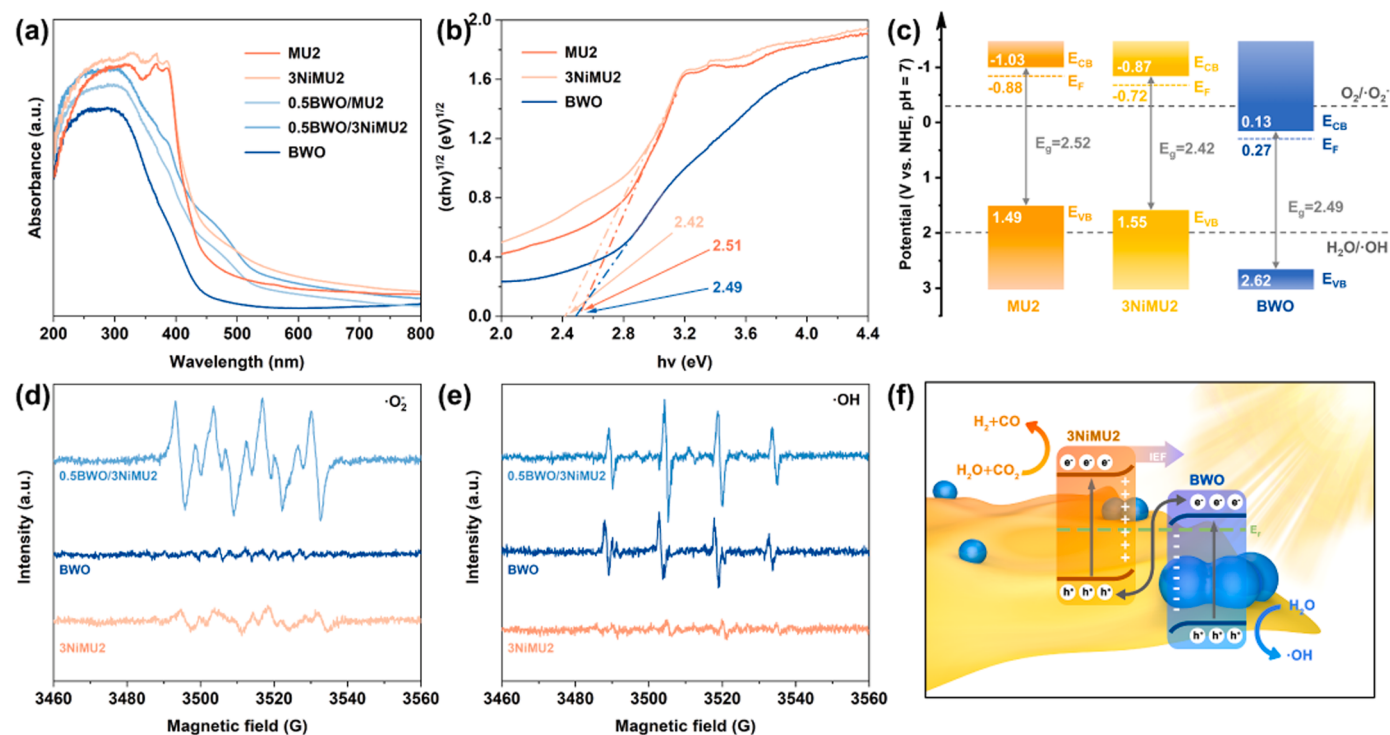


Fig. 4. (a) UV-visible diffuse reflectance spectra and (b) Tauc plots of the samples; (c) Band structure alignments of MU2, 3NiMU2 and BWO; EPR spin-trapping spectra recorded for (d) $\cdot\text{O}_2^-$ and (e) $\cdot\text{OH}$ under illumination for 3NiMU2, BWO and 0.5BWO/3NiMU2; (f) Schematic illustration of charge transfer route of the 0.5BWO/3NiMU2 heterojunction.

which may be due to the need of accumulation of photogenerated electrons or intermediates at the initial stage of the reaction [29,30]. The slight decay of activity after 8 h may result from the occurrence of re-adsorption or side reactions owing to the continuous accumulation of products [31,32]. In addition, the photothermal catalytic reaction was performed with Ar instead of CO₂ in order to demonstrate the absence of carbon sources other than CO₂. Fig. S14 shows that 0.5BWO/3NiMU2 can still rapidly drive the water splitting reaction to produce H₂, but no carbon products such as CO are detected. Without H₂O or catalyst, no gas-phase products are detected in the system. These results suggest that the reaction is the combination of CO₂ reduction with water oxidation, and the CO₂ introduced is the only carbon source of the produced CO.

To understand the roles of light and heat in the photothermal reaction, a series of control experiments were carried out. As shown in Fig. 3d, only a little CO and H₂ are generated in the first two-hour thermal catalytic reaction, while a rapid production of CO and H₂ can be immediately observed after introducing light irradiation, which indicates that light irradiation is one of the necessary conditions for highly efficient catalytic CO₂ reduction. Besides, the photothermal catalytic performance at different temperatures were investigated (Fig. 3e). It is obvious that the increase in system temperature not only improves the CO₂ conversion efficiency dramatically, but also has a great influence on the proportion of H₂ in the products. This is because as the temperature rises, the water from the bottom of the reactor will be gradually evaporated to gaseous H₂O. The increased concentration of gaseous H₂O makes it more easily adsorbed on the catalyst surface compared to the liquid state [33,34], which results in a strong competition with gaseous CO₂, and in turn promotes the production of H₂. Meanwhile, increased full-spectrum irradiation intensity also causes continuous enhancement in the photothermal CO₂ conversion efficiency of 0.5BWO/3NiMU2 (Fig. 3f). This suggests that the CO₂ reduction and H₂ evolution reactions are considerably influenced by the concentration of photogenerated electrons. The series of comparisons suggest that both single thermo- and photocatalysis are difficult to achieve high-efficiency CO₂ conversion, but photothermal synergistic effect can remarkably enhance the

catalytic activity of the photocatalysts.

3.3. Band structure and charge transfer mechanism

To reveal the reasons behind the great promotion of the catalytic performance by the construction of a heterojunction, the optical and photoelectrochemical properties as well as the charge transfer mechanism of the 0.5BWO/3NiMU2 heterojunction were investigated. From the UV-visible diffuse reflectance spectra shown in Fig. 4a, the introduction of Ni sites enhances the absorption of MU2 in the visible region, and the absorption edges of the heterojunctions are between those of BWO and PCN. The band gaps of MU2, 3NiMU2 and BWO are determined to be 2.51, 2.42 and 2.49 eV from the Tauc plots (Fig. 4b). The valence band (VB)-XPS spectra show that the contact potential differences (E_{VB}^*) between sample and the analyzer are 1.73, 1.79 and 2.86 eV, respectively (Fig. S15). According to the equation $E_{NHE}/V = \Phi + E_{VB}^* - 4.44$ [35,36], where the analyzer's electron work function Φ is 4.2 eV, the valence band maximum (E_{VB}) of MU2, 3NiMU2 and BWO are calculated to be 1.49, 1.55 and 2.62 V (vs. NHE, pH = 7). Based on the relationship between the band gap and the position of the band edge [37], it is deduced that the conduction band minimum (E_{CB}) of MU2, 3NiMU2 and BWO are -1.03 , -0.87 and 0.13 V (vs. NHE, pH = 7), respectively.

The Mott-Schottky plots were tested to estimate the Fermi level (E_F) of the semiconductors. The positive slopes of the Mott-Schottky plots (Fig. S16) reflect that MU2, 3NiMU2 and BWO are n-type semiconductors, and their flat-band potentials are -1.08 , -0.92 and 0.07 V (vs. Ag/AgCl, pH = 7), respectively. Since the flat-band potential of a semiconductor in the electrolytic solution approximately equals its E_F [38], the E_F of MU2, 3NiMU2 and BWO are calculated to be -0.88 , -0.72 and 0.27 V (vs. NHE, pH = 7) based on the Nerst equation $E_{NHE}/V = E_{Ag/AgCl}/V + 0.197$ V. The band structure alignments of MU2, 3NiMU2 and BWO are shown in Fig. 4c. It is obvious that 3NiMU2 has a staggered energy band position with BWO, which is necessary for the formation of an S-scheme heterojunction.

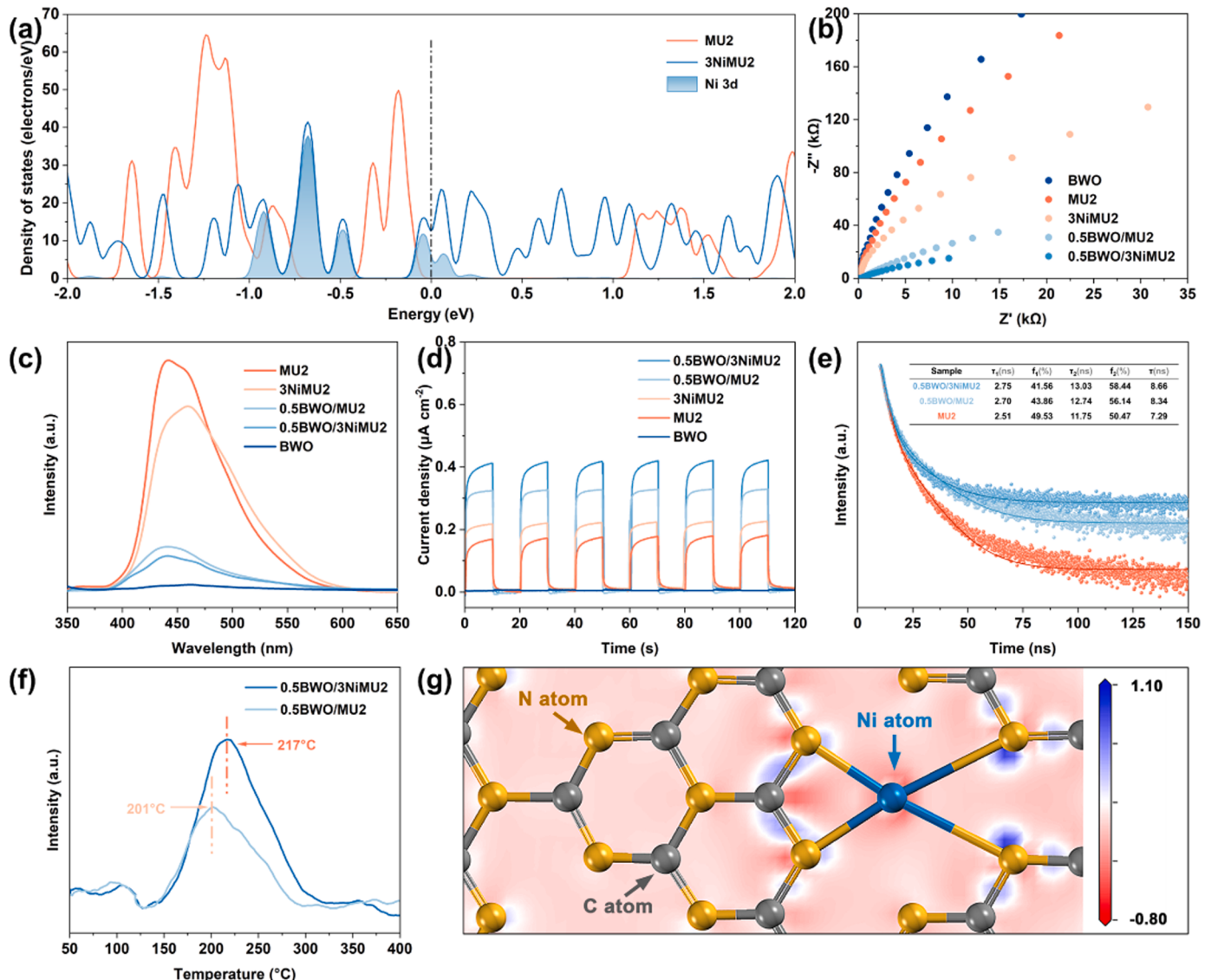


Fig. 5. (a) TDOS plots of MU2 and 3NiMU2 (the percentage of Ni 3d orbitals in 3NiMU2 is highlighted); (b) Nyquist plots, (c) steady-state PL spectra, (d) transient photocurrent response, (e) time-resolved PL spectra and (f) CO_2 -TPD profiles of the samples; (g) The electron density differences in 3NiMU2 (The blue and red colors represent the accumulation and depletion of electrons, respectively).

Electron paramagnetic resonance (EPR) spin-trapping tests can provide evidence for the formation of an S-scheme heterojunctions [39]. As a spin-trapping reagent, 5,5-dimethyl-1-pyrroline N-oxide (DMPO) can trap the superoxide radical ($\cdot\text{O}_2^-$) and hydroxyl radical ($\cdot\text{OH}$) in methanol and aqueous solutions, respectively [40]. In Fig. 4d, since the ECB of BWO and 3NiMU2 are more positive and more negative than the potential of $\text{O}_2/\cdot\text{O}_2^-$ (-0.33 V), respectively, the signal of DMPO- $\cdot\text{O}_2^-$ with the characteristic peak intensity ratio of 1:1:1:1 is detected only in the methanol solution with the addition of 3NiMU2. At the same time, as the E_{VB} of BWO is much more positive than the potential of $\text{H}_2\text{O}/\cdot\text{OH}$ (1.99 V), the aqueous solution with BWO shows a clear signal of DMPO-OH with a characteristic peak intensity ratio of 1:2:2:1 (Fig. 4e). In contrast, almost no DMPO-OH signal can be detected in the aqueous solution with 3NiMU2. It is noted that when 0.5BWO/3NiMU2 is added in the solutions, much stronger signals of either DMPO- $\cdot\text{O}_2^-$ or DMPO- $\cdot\text{OH}$ than those of any single semiconductor are detected, which means that more reactive species are produced under illumination. Meanwhile, no signals about any radicals are detected under dark (Fig. S17). This indicates that the construction of 0.5BWO/3NiMU2 heterojunction greatly enhances the redox capacity of both semiconductors. The above

results demonstrate the successful construction of an S-scheme heterojunction. In the photothermal catalytic reaction, the oxidation and reduction reactions occur at BWO and 3NiMU2 sides, respectively.

Based on the results of XPS spectra and EPR spin-trapping tests, we can elucidate the charge transfer mechanism of the 0.5BWO/3NiMU2 heterojunction. The higher E_F of 3NiMU2 compared to BWO will drive the spontaneous flow of electrons from 3NiMU2 to BWO until achieving a same E_F [41,42], resulting in the formation of an internal electric field (IEF) directing from 3NiMU2 to BWO. In this process, there will be an electron depletion layer and an electron-accumulating layer in the interfacial region at 3NiMU2 and BWO sides, respectively, which results in the upward and downward bending of their energy bands [43]. When light is injected, the IEF and the bending band will lead to the recombination of the photogenerated electrons in the CB of BWO and the photogenerated holes in the VB of 3NiMU2, following the S-scheme charge transfer route shown in Fig. 4f. This charge transfer mechanism effectively separates the photogenerated electron-hole pairs and maximizes the redox capacity of the photogenerated carriers. Therefore, the highly efficient overall reaction of CO_2 reduction with water oxidation was achieved.

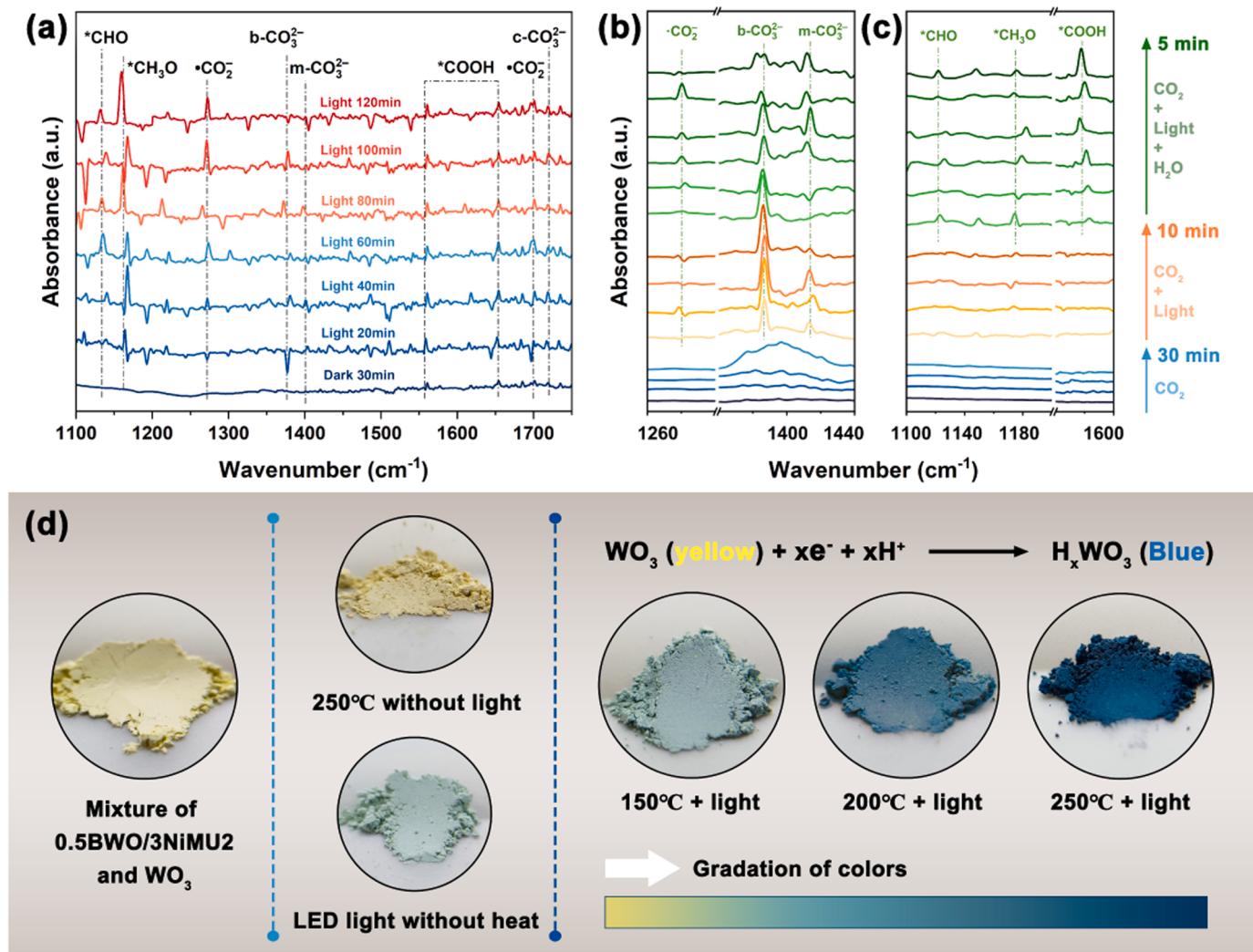


Fig. 6. (a) In-situ FT-IR spectra and transient FT-IR spectra of (b) CO₂ species and (c) key intermediates on 0.5BWO/3NiMU2. (d) Photographs of 0.5BWO/3NiMU2 and WO₃ mixture in the atmosphere of CO₂ and H₂O vapor after heat treatment or illumination.

3.4. Effects of atomically dispersed nickel sites

In order to reveal the effect of the atomically dispersed Ni sites on the catalytic performance, the band structures of MU2 and NiMU2 were investigated by density functional theory (DFT) calculations (Fig. 5a). The effect of Ni 3d orbitals leads to an increase of the total density of states (TDOS) at the E_{VB} of 3NiMU2 compared to MU2. This will make the electrons in the VB of 3NiMU2 more susceptible to be photo-excited to its CB [44]. In addition, the introduction of Ni sites results in a narrower band gap along with a higher density of states on the E_F, indicating that 3NiMU2 has stronger metallicity and enhanced electron transport ability [45], which can be evidenced by the Nyquist plots (Fig. 5b). The presence of Ni sites leads to a decrease in charge transfer resistance.

The carrier separation efficiency, which is another important factor affecting the photocatalytic activity, was tested by photoluminescence (PL) spectra and transient photocurrent response. As shown in Fig. 5c and d, the construction of heterojunction results in a sharp decrease in the PL peak intensity and an obvious increase in the photocurrent density, which can be attributed to the spatial separation of electron-hole pairs via the S-scheme charge transfer mechanism. The carrier separation efficiency of PCNs or heterojunctions was further improved after introducing Ni sites. In addition, the carrier lifetimes of the samples were obtained by fitting the data of time-resolved PL spectra with a

biexponential model (Fig. 5e). The short lifetime (τ_1) and long lifetime (τ_2) represent the radiative process of carrier recombination and the non-radiative process of energy transfer, respectively [39]. Obviously, 0.5BWO/3NiMU2 has prolonged τ_1 and τ_2 as well as a higher percentage of τ_2 compared to MU2 and 0.5BWO/MU2. The average lifetime (τ) of 0.5BWO/3NiMU2 is prolonged by 1.37 and 0.32 ns compared to the pristine PCN and 0.5BWO/MU2, respectively. The above results demonstrate that the introduction of Ni sites together with the construction of an S-scheme heterojunction effectively reduces the recombination of photogenerated carriers, so that more electrons and holes can participate in the surface reaction [46].

The enhanced catalytic activity by the introduction of Ni sites can be also associated with its contribution to CO₂ adsorption. From the CO₂-temperature-programmed desorption (TPD) profiles shown in Fig. 5f, the increase in peak area and the shift of the peak to the higher desorption temperature for 0.5BWO/NiMU2 compared to 0.5BWO/MU2 indicates that the Ni sites contribute to the stronger adsorption of more CO₂ molecules. In addition, the CO₂ adsorption amount of 0.5BWO/3NiMU2 is 87.45 $\mu\text{mol g}^{-1}$ as determined by thermogravimetric analysis (TGA), which is 1.68 times that of 0.5BWO/MU2 (Fig. S18). Fig. 5g shows the change of electron density of atoms within PCN after the introduction of Ni sites. It can be seen that an electric field pointing from Ni to N atoms is formed after the Ni atoms enter the heptazine rings of PCN. This coincides with the result from XPS spectra that the N 1 s peaks

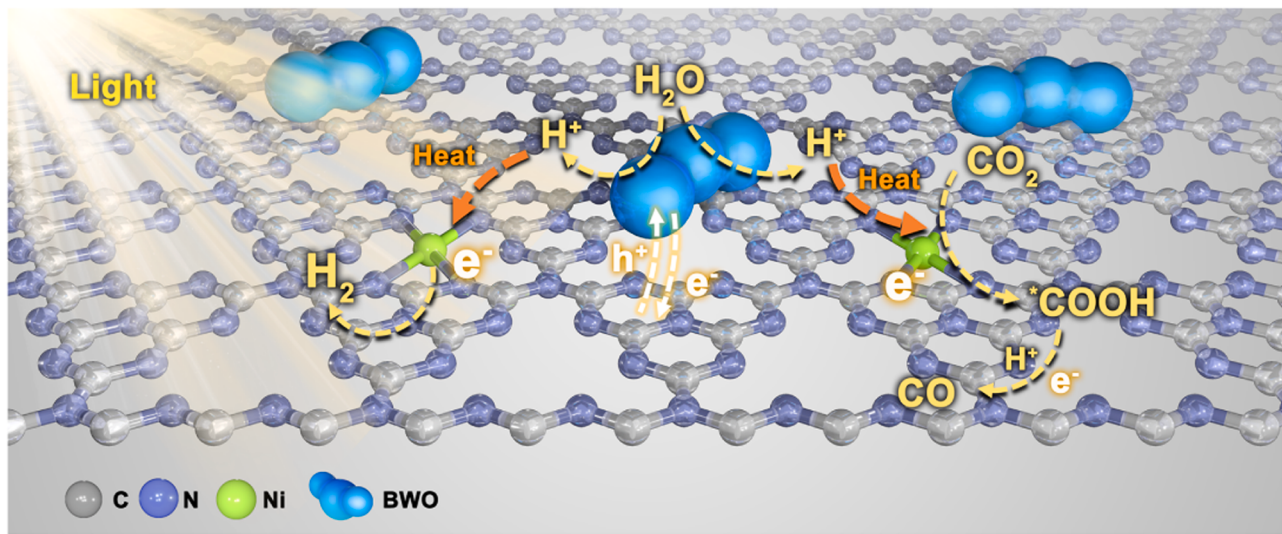


Fig. 7. Schematic illustration of possible syngas production pathways over 0.5BWO/3NiMU2 heterojunction under photothermal condition.

of 3NiMU2 shift to the lower binding energy compared to MU2. With the influence of this electric field, the photogenerated electrons will be transferred from the neighboring N atoms to the Ni atoms, which promote charge separation as well as the adsorption, activation and reduction of CO₂ on the Ni sites [47]. Therefore, the Ni sites not only promote the charge separation and transport ability of the catalyst, but also facilitate the adsorption and reduction of CO₂ as active sites through gathering photogenerated electrons.

3.5. Mechanisms of photothermal CO₂ conversion with H₂O

In order to detect the adsorption, activation and conversion of CO₂ during the photothermal catalytic reaction, the behavior of the gas molecules was recorded with an in-situ dual-beam FT-IR spectrometer in H₂O vapor and CO₂ atmospheres at 250 °C. As shown in Fig. 6a, the peaks at 1380, 1400 and 1720 cm⁻¹ are monodentate carbonate (m-CO₃²⁻), bidentate carbonate (b-CO₃²⁻) and chelating-bridged carbonate (c-CO₃²⁻), respectively. The peaks at 1280 and 1700 cm⁻¹ are attributed to adsorbed·CO₂ [48,49]. The peaks at 1560 and 1655 cm⁻¹ belong to the *COOH group (* represents the adsorption state on the photocatalyst surface), which is generally regarded as a key intermediate in the photoreduction of CO₂ to CO or CH₄. In addition, the absorbance peaks at 1132 and 1160 cm⁻¹ can be assigned to the signals of *CHO and *CH₃O [50–52], which are also intermediates for CO₂ conversion to CH₄. The intensity of the above peaks increases with the irradiation duration, which reflects a continuous adsorption, activation and reduction process on the catalyst surface.

In addition, transient FT-IR experiment was carried out to validate the key species driving the conversion of CO₂. CO₂ was first passed into the reaction cell at 250 °C in dark, followed by sequentially turning on the light source and introducing H₂O vapor. As shown in Fig. 6b, a wide peak related to absorbed CO₂ is observed at around 1400 cm⁻¹ at the first stage. When the light was turned on, the peaks corresponding to ·CO₂ and carbonate species such as b-CO₃²⁻ and m-CO₃²⁻ can be quickly observed in the spectra, which implies the activation of CO₂ molecules by photogenerated electrons. Moreover, the concentration of CO₂ species increases with prolonging illumination time, but the key intermediates do not appear. After the introduction of H₂O vapor, the concentration of CO₂ species decreases rapidly, while the peaks of key intermediates such as *CHO, *CH₃O and *COOH are emerged and gradually enhanced (Fig. 6c), suggesting the initiation of CO₂ reduction reaction. These results indicate that the CO₂ photothermal conversion is a light-driven proton-coupled electron reduction process, in which

H₂O or rather H⁺ is an essential part of the reaction.

Since H⁺ is necessary in photothermal CO₂ conversion for the production of CO and H₂, the detection of H⁺ produced during the reaction can provide insight into the photothermal synergistic mechanism. The generation of H⁺ can be visually reflected by the color change of 0.5BWO/3NiMU2 and WO₃ mixture using WO₃ as a probe of H⁺, because yellow WO₃ will transform to dark blue H_xWO₃ after being contacted with H⁺ [53–55]. As shown in Fig. 6d, the color of the mixture does not change when the temperature is increased to 250 °C in dark, which indicates that only heat is not sufficient to trigger water splitting. By contrast, after 15 min of illumination with a 420 nm LED light at room temperature, the color of the mixture transforms to light blue. It should be noted that due to the very low intensity of the LED light, the temperature during this process was almost unchanged (Fig. S19), and therefore heat effect can be negligible in this case. The above comparison confirms that light is the key to trigger the splitting of water and the generation of H⁺. Furthermore, when the mixture was exposed to light for the same duration but at different temperatures, it can be clearly seen that the color of the mixture gradually deepens as the temperature rises. This suggests that the increase in temperature can significantly promote the generation and diffusion of H⁺. It can be concluded that the H⁺ that is essential for producing CO and H₂ should be induced by light, therefore, light is the indispensable driving force for the conversion of CO₂ to syngas, while heat can efficiently promote the spillover of the H⁺ generated via water oxidation to the Ni sites of 3NiMU2, thus greatly accelerating the reaction rate of CO₂ reduction and H₂ evolution.

Based on the above analysis, the process of converting CO₂ and H₂O to syngas via photothermal catalysis is shown in Fig. 7. During this process, the introduced single Ni sites acting as active sites enhances the adsorption and activation of CO₂ molecules on the catalyst surface. The S-scheme heterojunction with high carrier separation efficiency provides sufficient photogenerated electrons under illumination. Adsorbed CO₂ molecules are first activated to ·CO₂ and carbonate species by photogenerated electrons. After the dissociation of H₂O driven by light, the resulting H⁺ rapidly diffuses to the Ni sites of 3NiMU2 for the CO₂ reduction or H₂ evolution reactions under the effect of heat. The activated CO₂ species are then coupled with H⁺ to produce the key intermediate *COOH, which is further hydrogenated to generate CO. Continuous heating promotes the generation and diffusion of a large amount of H⁺ during the reaction process. The favorable active sites coupled with the continuous supply of photogenerated electrons and H⁺ induced by light and input heat ensures the highly efficient conversion of CO₂ and H₂O to syngas.

4. Conclusions

In summary, an S-scheme heterojunction composed of single Ni sites embedded ultrathin crystalline PCN nanosheets and Bi_2WO_6 nanoparticles was constructed. The heterojunction catalyst can efficiently photoconvert CO_2 and H_2O to syngas at a medium temperature of 250 °C with CO and H₂ production rates of 4493 and 9191 $\mu\text{mol g}^{-1} \text{h}^{-1}$, respectively, much higher than those of the reported photo- or photothermal CO_2 conversion catalysts. The S-scheme charge transfer route greatly improves the charge separation efficiency and redox capacity of the catalyst, while the introduction of atomically dispersed Ni sites further promotes the charge transfer efficiency and enhances the CO_2 adsorption capacity. Moreover, the photothermal synergistic effect during CO_2 conversion as well as the reaction route was revealed. This work provides a promising strategy for efficient photoconversion of CO_2 and H_2O to syngas under mild conditions, and exemplifies the design of high-performance photothermal catalysts for CO_2 conversion.

CRediT authorship contribution statement

Guo Xinwen: Writing – review & editing, Supervision, Funding acquisition. **Song Chunshan:** Writing – review & editing, Supervision. **Liu Jiaxu:** Investigation. **Yan Siyang:** Investigation. **An Sufeng:** Investigation. **Li Keyan:** Writing – review & editing, Supervision, Funding acquisition, Conceptualization. **Wu Jiaming:** Writing – original draft, Methodology, Investigation, Data curation.

Declaration of Competing Interest

The authors declare that they have no known competing financial interests or personal relationships that could have appeared to influence the work reported in this paper.

Data availability

Data will be made available on request.

Acknowledgements

This work was supported by the Natural Science Foundation of Liaoning Province (2022-MS-131), the National Natural Science Foundation of China (22278056, 22202029), the Fundamental Research Funds for the Central Universities (DUT22LAB602), the National Key Research and Development Program of China (2022YFA1504402), the Liaoning Revitalization Talents Program (XLYC2008032) and the China Postdoctoral Science Foundation (2023T160716).

Appendix A. Supporting information

Supplementary data associated with this article can be found in the online version at [doi:10.1016/j.apcatab.2024.123822](https://doi.org/10.1016/j.apcatab.2024.123822).

References

- [1] L. Sun, Z. Zhang, J. Bian, F. Bai, H. Su, Z. Li, J. Xie, R. Xu, J. Sun, L. Bai, C. Chen, Y. Han, J. Tang, L. Jing, A Z-scheme heterojunctional photocatalyst engineered with spatially separated dual redox sites for selective CO_2 reduction with water: Insight by in-situ micros-transient absorption spectra, *Adv. Mater.* 35 (2023) e2300064.
- [2] J. Yu, L. Huang, Q. Tang, S. Yu, Q. Qi, J. Zhang, D. Ma, Y. Lei, J. Su, Y. Song, J. Eloi, R.L. Harniman, U. Borucu, L. Zhang, M. Zhu, F. Tian, L. Du, D.L. Phillips, I. Manners, R. Ye, J. Tian, Artificial spherical chromatophore nanomicelles for selective CO_2 reduction in water, *Nat. Catal.* 6 (2023) 464–475.
- [3] X. Liu, S. Inagaki, J. Gong, Heterogeneous molecular systems for photocatalytic CO_2 reduction with water oxidation, *Angew. Chem. Int. Ed.* 55 (2016) 14924–14950.
- [4] T. Liu, W. Li, D.Z. Wang, T. Luo, M. Fei, D. Shin, M.M. Waegele, D. Wang, Low catalyst loading enhances charge accumulation for photoelectrochemical water splitting, *Angew. Chem. Int. Ed.* 62 (2023) e202307909.
- [5] P. Li, L. Liu, W. An, H. Wang, H. Guo, Y. Liang, W. Cui, Ultrathin porous g-C₃N₄ nanosheets modified with AuCu alloy nanoparticles and C-C coupling photothermal catalytic reduction of CO to ethanol, *Appl. Catal. B: Environ.* 266 (2020) 118618.
- [6] F. Fresno, A. IglesiasJuez, J.M. Coronado, Photothermal catalytic CO_2 conversion: beyond catalysis and photocatalysis, *Top. Curr. Chem.* 381 (2023) 21.
- [7] J. Yan, C. Wang, H. Ma, Y. Li, Y. Liu, N. Suzuki, C. Terashima, A. Fujishima, X. Zhang, Photothermal synergic enhancement of direct Z-scheme behavior of $\text{Bi}_4\text{TaO}_8\text{Cl}/\text{W}_{18}\text{O}_{49}$ heterostructure for CO_2 reduction, *Appl. Catal. B: Environ.* 268 (2020) 118401.
- [8] S. Ning, H. Ou, Y. Li, C. Lv, S. Wang, D. Wang, J. Ye, $\text{Co}^{0+}\text{-Co}^{\delta+}$ interface double-site-mediated C-C coupling for the photothermal conversion of CO_2 into light olefins, *Angew. Chem. Int. Ed.* 62 (2023) e202302253.
- [9] Q. Hao, Z. Li, Y. Shi, R. Li, Y. Li, L. Wang, H. Yuan, S. Ouyang, T. Zhang, Plasmon-induced radical-radical heterocoupling boosts photodriven oxidative esterification of benzyl alcohol over nitrogen-doped carbon-encapsulated cobalt nanoparticles, *Angew. Chem. Int. Ed.* 62 (2023) e202312808.
- [10] F.K. Kessler, Y. Zheng, D. Schwarz, C. Merschjann, W. Schnick, X. Wang, M. JoBojdys, Functional carbon nitride materials design strategies for electrochemical devices, *Nat. Rev. Mater.* 2 (2017) 1–17.
- [11] X. Chi, Z.A. Lan, Q. Chen, X. Zhang, X. Chen, G. Zhang, X. Wang, Electronic transmission channels promoting charge separation of conjugated polymers for photocatalytic CO_2 reduction with controllable selectivity, *Angew. Chem. Int. Ed.* 62 (2023) e202303785.
- [12] G. Rocha, M.A.R. da Silva, A. Rogolino, G.A.A. Diab, L.F.G. Noleto, M. Antonietti, I. F. Teixeira, Carbon nitride based materials: More than just a support for single-atom catalysis, *Chem. Soc. Rev.* 52 (2023) 4878–4932.
- [13] P. Liu, Z. Huang, X. Gao, X. Hong, J. Zhu, G. Wang, Y. Wu, J. Zeng, X. Zheng, Synergy between palladium single atoms and nanoparticles via hydrogen spillover for enhancing CO_2 photoreduction to CH_4 , *Adv. Mater.* 34 (2022) e2200057.
- [14] L. Cheng, X. Yue, L. Wang, D. Zhang, P. Zhang, J. Fan, Q. Xiang, Dual-single-atom tailoring with bifunctional integration for high-performance CO_2 photoreduction, *Adv. Mater.* 33 (2021) e2105135.
- [15] H. Chand, A. Kumar, S. Goswami, V. Krishnan, Comparison of catalytic activity of graphitic carbon nitrides derived from different precursors for carbon dioxide conversion, *Fuel* 357 (2024) 129757.
- [16] L.S. Gómez-Velázquez, L. Madriz, M. Rigoletto, E. Laurenti, M. Bizarro, M. L. Dell'Arciprete, M.C. González, Structural and physicochemical properties of carbon nitride nanoparticles via precursor thermal treatment: effect on methyl orange photocatalytic discoloration, *ACS Appl. Nano Mater.* 6 (2023) 14049–14062.
- [17] M. Zhang, P. Huang, J.P. Liao, M.Y. Yang, S.B. Zhang, Y.F. Liu, M. Lu, S.L. Li, Y. P. Cai, Y.Q. Lan, Relative local electron density tuning in metal-covalent organic frameworks for boosting CO_2 photoreduction, *Angew. Chem. Int. Ed.* 62 (2023) e202311999.
- [18] T. Chen, L. Liu, C. Hu, H. Huang, Recent advances on Bi_2WO_6 -based photocatalysts for environmental and energy applications, *Chin. J. Catal.* 42 (2021) 1413–1438.
- [19] M. Xiao, Z. Wang, M. Lyu, B. Luo, S. Wang, G. Liu, H.M. Cheng, L. Wang, Hollow nanostructures for photocatalysis: advantages and challenges, *Adv. Mater.* 31 (2019) e1801369.
- [20] S. Bera, S. Samajdar, S. Pal, P.S. Das, L.A.H. Jones, H. Finch, V.R. Dhanak, S. Ghosh, Effect of metal doping in Bi_2WO_6 micro-flowers for enhanced photoelectrochemical water splitting, *Ceram. Int.* 48 (2022) 35814–35824.
- [21] X. Lian, W. Xue, S. Dong, E. Liu, H. Li, K. Xu, Construction of S-scheme $\text{Bi}_2\text{WO}_6/\text{g-C}_3\text{N}_4$ heterostructure nanosheets with enhanced visible-light photocatalytic degradation for ammonium dinitramide, *J. Hazard. Mater.* 412 (2021) 125217.
- [22] W. He, Y. Sun, G. Jiang, H. Huang, X. Zhang, F. Dong, Activation of amorphous Bi_2WO_6 with synchronous Bi metal and Bi_2O_3 coupling: Photocatalysis mechanism and reaction pathway, *Appl. Catal. B: Environ.* 232 (2018) 340–347.
- [23] J. Li, C. Yu, W. Fang, L. Zhu, W. Zhou, Q. Fan, Preparation, characterization and photocatalytic performance of heterostructured $\text{AgCl}/\text{Bi}_2\text{WO}_6$ microspheres, *Chin. J. Catal.* 36 (2015) 987–993.
- [24] X. Wang, X. Liu, H. Wen, K. Guo, H. Brendon, D. Liu, A green, efficient reductive N-formylation of nitro compounds catalyzed by metal-free graphitic carbon nitride supported on activated carbon, *Appl. Catal. B: Environ.* 321 (2023) 122042.
- [25] C. Pulignani, C.A. Mesa, S.A.J. Hillman, T. Uekert, S. Gimenez, J.R. Durrant, E. Reisner, Rational design of carbon nitride photoelectrodes with high activity toward organic oxidations, *Angew. Chem. Int. Ed.* 61 (2022) e202211587.
- [26] G. Yan, X. Sun, Y. Zhang, H. Li, H. Huang, B. Jia, D. Su, T. Ma, Metal-free 2D/2D van der Waals heterojunction based on covalent organic frameworks for highly efficient solar energy catalysis, *Nanomicro. Lett.* 15 (2023) 132.
- [27] S. Gao, L. Pan, W. Kong, L. Zhou, J. Wu, S. Zhou, W. Shi, F. Yang, Y. Kong, Engineering in-plane π -conjugated structures in ultrathin g-C₃N₄ nanosheets for enhanced photocatalytic reduction performance, *Appl. Surf. Sci.* 610 (2023) 155574.
- [28] J. Wu, L. Xiong, Y. Hu, Y. Yang, X. Zhang, T. Wang, Z. Tang, A. Sun, Y. Zhou, J. Shen, Z. Zou, Organic half-metal derived erythroid-like $\text{BiVO}_4/\text{hm-C}_4\text{N}_3$ Z-Scheme photocatalyst: Reduction sites upgrading and rate-determining step modulation for overall CO_2 and H_2O conversion, *Appl. Catal. B: Environ.* 295 (2021) 120277.
- [29] S. Yang, W. Hu, X. Zhang, P. He, B. Pattengale, C. Liu, M. Cendejas, I. Hermans, X. Zhang, J. Zhang, J. Huang, 2D covalent organic frameworks as intrinsic photocatalysts for visible light-driven CO_2 reduction, *J. Am. Chem. Soc.* 140 (2018) 14614–14618.

- [30] K. Sekizawa, K. Maeda, K. Domen, K. Koike, O. Ishitani, Artificial Z-scheme constructed with a supramolecular metal complex and semiconductor for the photocatalytic reduction of CO₂, J. Am. Chem. Soc. 135 (2013) 4596–4599.
- [31] E. Gong, S. Ali, C.B. Hiragond, H.S. Kim, N.S. Powar, D. Kim, H. Kim, S.-I. In, Solar fuels: Research and development strategies to accelerate photocatalytic CO₂ conversion into hydrocarbon fuels, Energy Environ. Sci. 15 (2022) 880–937.
- [32] S. Fang, M. Rahaman, J. Bharti, E. Reisner, M. Robert, G.A. Ozin, Y.H. Hu, Photocatalytic CO₂ reduction, Nat. Rev. Methods Prim. 3 (2023) 61.
- [33] S. Xie, C. Deng, Q. Huang, C. Zhang, C. Chen, J. Zhao, H. Sheng, Facilitated photocatalytic CO₂ reduction in aerobic environment on a copper-porphyrin metal-organic framework, Angew. Chem. Int. Ed. 62 (2023) e202216717.
- [34] J. Li, L. Ding, Z. Su, K. Li, F. Fang, R. Sun, Y. Qin, K. Chang, Non-Lignin constructing the gas-solid interface for enhancing the photothermal catalytic water vapor splitting, Adv. Mater. 35 (2023) e2305535.
- [35] J. Wu, K. Li, S. Yang, C. Song, X. Guo, *In-situ* construction of BiOBr/Bi₂WO₆ S-scheme heterojunction nanoflowers for highly efficient CO₂ photoreduction: regulation of morphology and surface oxygen vacancy, Chem. Eng. J. 452 (2023) 139493.
- [36] L. Wang, L. Zhang, B. Lin, Y. Zheng, J. Chen, Y. Zheng, B. Gao, J. Long, Y. Chen, Activation of carbonyl oxygen sites in beta-ketoamine-linked covalent organic frameworks via cyano conjugation for efficient photocatalytic hydrogen evolution, Small 17 (2021) 2101017.
- [37] H. Deng, X. Fei, Y. Yang, J. Fan, J. Yu, B. Cheng, L. Zhang, S-scheme heterojunction based on p-type ZnMn₂O₄ and n-type ZnO with improved photocatalytic CO₂ reduction activity, Chem. Eng. J. 409 (2021) 127377.
- [38] M.A. Zabara, B. Yarar Kaplan, S. Alkan Gürsel, A. Yürüm, Facet-dependent interfacial and photoelectrochemical properties of TiO₂ nanoparticles, Adv. Mater. Interfaces 10 (2023) 2300555.
- [39] P. Xia, S. Cao, B. Zhu, M. Liu, M. Shi, J. Yu, Y. Zhang, Designing a 0D/2D S-scheme heterojunction over polymeric carbon nitride for visible-light photocatalytic inactivation of bacteria, Angew. Chem. Int. Ed. 59 (2020) 5218–5225.
- [40] W. Zhang, S. Zhao, Y. Xing, H. Qin, Q. Zheng, P. Zhang, S. Zhang, X. Xu, Sandwich-like P-doped h-BN/ZnIn₂S₄ nanocomposite with direct Z-scheme heterojunction for efficient photocatalytic H₂ and H₂O₂ evolution, Chem. Eng. J. 442 (2022) 136151.
- [41] C. Cheng, B. He, J. Fan, B. Cheng, S. Cao, J. Yu, An inorganic/organic S-scheme heterojunction H₂-production photocatalyst and its charge transfer mechanism, Adv. Mater. 33 (2021) 2100317.
- [42] X. Wu, G. Chen, J. Wang, J. Li, G. Wang, Review on S-scheme heterojunctions for photocatalytic hydrogen evolution, Acta Phys. Chim. Sin. 39 (2023) 2212016.
- [43] L. Zhang, J. Zhang, H. Yu, J. Yu, Emerging S-scheme photocatalyst, Adv. Mater. 34 (2022) e2107668.
- [44] L. Ran, Z. Li, B. Ran, J. Cao, Y. Zhao, T. Shao, Y. Song, M.K.H. Leung, L. Sun, J. Hou, Engineering single-atom active sites on covalent organic frameworks for boosting CO₂ photoreduction, J. Am. Chem. Soc. 144 (2022) 17097–17109.
- [45] W. Liu, S. Niu, Z. Xu, R. Zou, C. Cui, Y. Lei, X. Zhang, F. Ran, Highly-dispersed nickel on 2D graphitic carbon nitrides (g-C₃N₄) for facilitating reaction kinetics of lithium-sulfur batteries, Appl. Surf. Sci. 609 (2023) 155327.
- [46] K. Lu, F. Xue, F. Liu, M. Li, W. Fu, H. Peng, C. Zhang, J. Huang, Z. Gao, H. Huang, M. Liu, N-NaTaO₃@Ta₃N₅ core-shell heterojunction with controlled interface boosts photocatalytic overall water splitting, Adv. Energy Mater. 13 (2023) 2301158.
- [47] G. Liu, G. Dong, Y. Zeng, C. Wang, The photocatalytic performance and active sites of g-C₃N₄ effected by the coordination doping of Fe(III), Chin. J. Catal. 41 (2020) 1564–1572.
- [48] J. Sheng, Y. He, J. Li, C. Yuan, H. Huang, S. Wang, Y. Sun, Z. Wang, F. Dong, Identification of halogen-associated active sites on bismuth-based perovskite quantum dots for efficient and selective CO₂-to-CO photoreduction, ACS Nano 14 (2020) 13103–13114.
- [49] H. Shi, H. Wang, Y. Zhou, J. Li, P. Zhai, X. Li, G.G. Gurzadyan, J. Hou, H. Yang, X. Guo, Atomically dispersed indium-copper dual-metal active sites promoting C-C coupling for CO₂ photoreduction to ethanol, Angew. Chem. Int. Ed. 61 (2022) e202208904.
- [50] J. Xu, Z. Ju, W. Zhang, Y. Pan, J. Zhu, J. Mao, X. Zheng, H. Fu, M. Yuan, H. Chen, R. Li, Efficient infrared-light-driven CO₂ reduction over ultrathin metallic Ni-doped CoS₂ nanosheets, Angew. Chem. Int. Ed. 60 (2021) 8705–8709.
- [51] L. Cheng, X. Yue, J. Fan, Q. Xiang, Site-specific electron-driving observations of CO₂-to-CH₄ photoreduction on Co-doped CeO₂/crystalline carbon nitride S-scheme heterojunctions, Adv. Mater. 34 (2022) 2200929.
- [52] J.P. Dong, Y. Xu, X.G. Zhang, H. Zhang, L. Yao, R. Wang, S.Q. Zang, Copper-sulfur-nitrogen cluster providing a local proton for efficient carbon dioxide photoreduction, Angew. Chem. Int. Ed. 62 (2023) e202313648.
- [53] D. Yoon, A. Manthiram, Hydrogen tungsten bronze as a decoking agent for long-life, natural gas-fueled solid oxide fuel cells, Energy Environ. Sci. 7 (2014) 3069–3076.
- [54] H. Ji, X. Wang, X. Wei, Y. Peng, S. Zhang, S. Song, H. Zhang, Boosting polyethylene hydrogenolysis performance of Ru-CeO₂ catalysts by finely regulating the Ru sizes, Small 19 (2023) e2300903.
- [55] Y. Chen, Y. Zhang, G. Fan, L. Song, G. Jia, H. Huang, S. Ouyang, J. Ye, Z. Li, Z. Zou, Cooperative catalysis coupling photo-/photothermal effect to drive Sabatier reaction with unprecedented conversion and selectivity, Joule 5 (2021) 3235–3251.